TÉCNICO LISBOA

Control of Cyber-physical Systems

LABORATORY WORK REPORT — PART I

Identification of a Flexible Robot Arm Joint

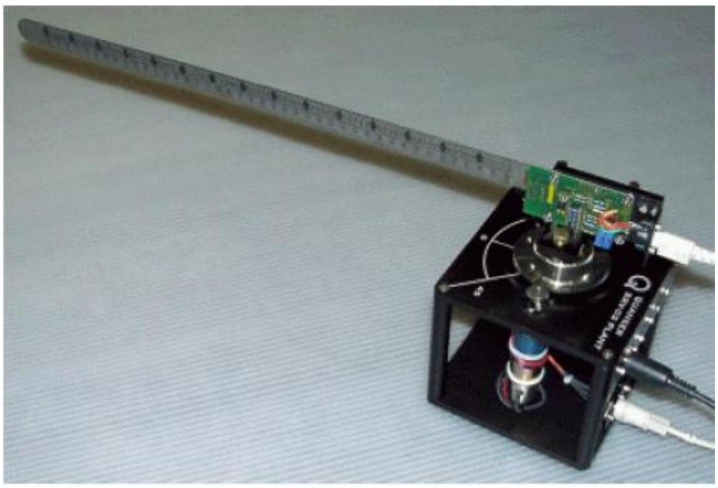

Shift CSCib-2L03

Group 09:
Abdelrahman Abdelhamed — IST1114981
Marina Gabarda López — IST1114980
Shahriar Hassan — IST1114979

2024/2025 – 1st Quarter

Instituto Superior Técnico
Department of Electrical and Computer Engineering
Scientific Area of Systems, Decision, and Control

Contents

Introduction

The setup features a motor aligned vertically with a flexible bar connected to it. The angle of the axis is measured using a Potentiometer, while a Strain Gauge assesses the deflection of the bar. The calibration of these sensors establishes two constants crucial for the measurement systems. The arm's motor is linked to the angular position of its tip through a plant model, which will be utilized for future controller design.

1 Question 1 - Analyzing the problem

1.1 Why is achieving this control objective nontrivial? (2.5 pts)

Achieving the control objective is nontrivial due to several complexities in the system's dynamics and measurement limitations. The motor's speed is controlled by voltage, not position, and inaccuracies in the model make it difficult to achieve precise control without feedback. Additionally, the system is prone to overshooting and vibrations, even with ideal conditions. The presence of complex conjugate poles and the interaction between subsystems further complicates control, as the behavior of the entire system is influenced by the poles of both subsystems. Moreover, the inability to directly measure the tip location adds to the challenge, making the control problem more intricate and difficult to solve.

2 Question 2 - Interfacing the plant with the computer (5 pts)

2.1 Comment on the motor operation. Explain in particular why their angular position never stabilizes when its command signal is constant in the open loop conditions described. (0.5 pts)

The motor's velocity is controlled by applied voltage, ensuring constant angular velocity with continuous monitoring. With the motor shaft vertical, gravity's impact is minimal. Achieving precise positioning without feedback is challenging due to model inaccuracies and disturbances, even with stable reference signals. Impulses to the motor may cause overshooting and minimal damping.

The system is segmented to simplify pole estimation. We hypothesize the integrator's poles are at the s-plane origin, while another segment shows a complex conjugate pole pair in the s-plane's left plane. Roughly identifying these poles is crucial as the system's division allows simpler analysis, yet retaining complexity when subsystems connect serially. Each subsystem's poles reflect in the overall system. The complexity of controlling tip position without direct measurement is discussed in subsequent sections, emphasizing the control objective's significance.

2.2 Explain the procedure carried out to perform sensor calibration. (4.5 pts)

The DC motor, mounted on the Rotary Servo Base Unit, rotates the attached flexible link within a horizontal plane, crucial for precise angle control and link deflection measurements. At the junction where the motor and link connect, a strain gauge measures deflections at the link's tip, with its output being directly proportional to the deflection magnitude. The link's deflection angle increases positively with counterclockwise (CCW) rotation, as does the potentiometer reading, denoted by θ. The servo rotates CCW when subjected to a positive control voltage. In an open-loop setup, the DC servo motor operates on a constant command signal. This approach lacks accuracy in controlling the motor's angular position due to the absence of feedback and external disturbances like drift, load changes, and voltage fluctuations, causing cumulative errors and preventing stable angular positioning. To enhance control accuracy and stability, a closed-loop system is essential. It employs continuous feedback from sensors to monitor and adjust deviations, ensuring more reliable motor operation.

A Simulink block diagram, shown in Figure (1), was created to manage signal transmission to the motor. It includes a signal generator, an analog output block for signal dispatch, a scope for recording, and two analog input blocks to display sensor data, accommodating the two sensors in the system.

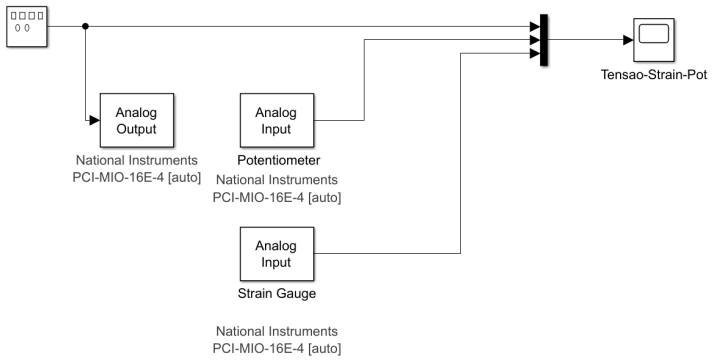

Figure 1: Simulink Block Diagram

2.3 Calibration of Potentiometer model

A potentiometer is utilized for the measurement of the shaft angle. The device includes a cursor that moves along a resistive wire, modifying the resistance proportionally to the angle of rotation. This variation in resistance is transformed by an electrical circuit into a voltage measurement. As a result, the shaft angle θ can be approximated by the following function of the sensor output θ_e:

$$\theta = \theta_e K_p$$

Here, K_p is a constant with dimensions of [degrees/V]. To obtain the voltage (tensions) at different angles, we performed one 360 degree rotation and recorded the output voltages as shown in Table 1 shows the shaft angle θ and the sensor output θ_e.

The slope of the voltage versus angle curve, illustrated in Figure 2, provides the value of K_p. The experimental determination of K_p yielded a value of 35.3218 degrees/V.

Table 1: Potentiometer readings

θ (degree)	θ_e (V)
0	-5.1025
180	-0.0048
360	5.092

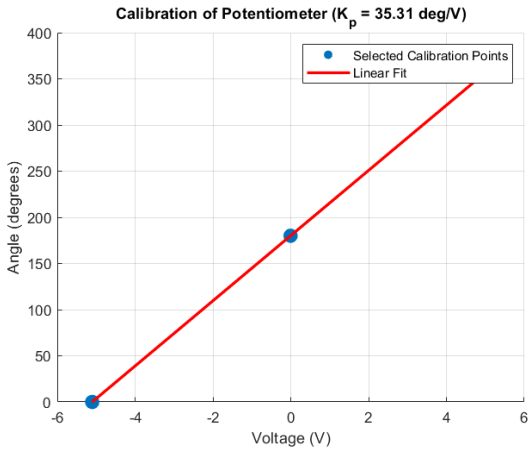

Figure 2: Plot of tension against angles for K_p

2.4 Calibration of Strain Gauge model

To measure the approximate value of K_e, we did several experiments as mentioned in the lab manual. The flexible bar was supported by a stand. We used a "comb" to deflect the bar at a certain distance $40cm$. The comb has multiple slots spaced $\frac{1}{4}$ inch apart. We assumed the center slot as the 0^{th} slot and measured the distance on both sides. Here, we carefully considered the angle. We assumed the left side of the comb produced the negative angle and vice-versa. It created a right-angle triangle and we calculated the corresponding angle α of each triangle using the Pythagoras method. Following is the data table for the calculated values of α and measured values of K_e:

α (degree)	V (Volts)
1.81	1.5
3.63	2.7
5.44	3.8
-1.81	-1.0
-3.63	-2.2
-5.44	-3.3

Table 2: Values of α (degree) and Tension (V)

We used the linear regression model to find the best-fitted line and estimated the value. We found, K_e = **1.34 deg/V**

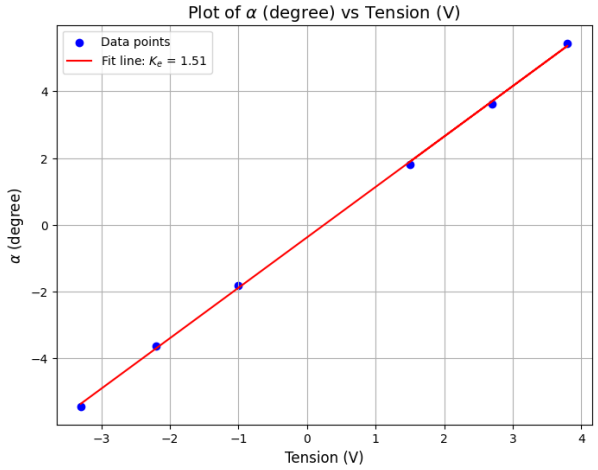

Figure 3: Linear Regression Model of α (degree) and Tension (V)

3 Question 3 - Model identification and validation (9.5 pts)

3.1 Explanation on the tests performed on the plant to obtain the data used for identification. Discuss the results obtained with different types of excitation signals and the effect of very small amplitude and very large amplitude excitation signals. (2 pts)

Several experiments were conducted on the plant using two excitation signals to gather data for system model identification, focusing on understanding the dynamic behavior and responses of the system.

Initially, we applied **Square Wave signal (amp=**$1.5V$**) and (amp=**$2V$**)**, which are useful for observing the system's response to sudden changes. This helped us gain insights into its transient behavior and steady-state dynamics. However, square waves were found to be limited as they only excited the system within a narrow frequency range, restricting the breadth of system response data. To overcome the limitations of square waves, we shifted to using **Pseudo Random Binary Sequences signal (PRBS) (amp=**$1.5V$**)** . PRBS signals, with their random nature, excite a broader frequency spectrum, providing a comprehensive view of the plant's dynamics. This ensured the capture of both low and high-frequency components, enhancing the robustness of the ARMAX model over what was possible with periodic signals like square waves alone.

During testing, we identified that a higher excitation frequency improved system response visualization. We adjusted the PRBS frequency to $0.8H_z$ and the square wave to $0.6H_z$ Figure 4 to more accurately capture the behavior of the system, particularly noting the intensified deflection of the flexible bar with direction changes. Furthermore, amplitude adjustments revealed critical limitations: very low amplitudes were insufficient for moving the bar due to low motor torque, failing to overcome inertia and friction, which resulted in inadequate data. Conversely, very high amplitudes induced nonlinearities such as motor saturation and excessive mechanical stress, distorting the collected data.

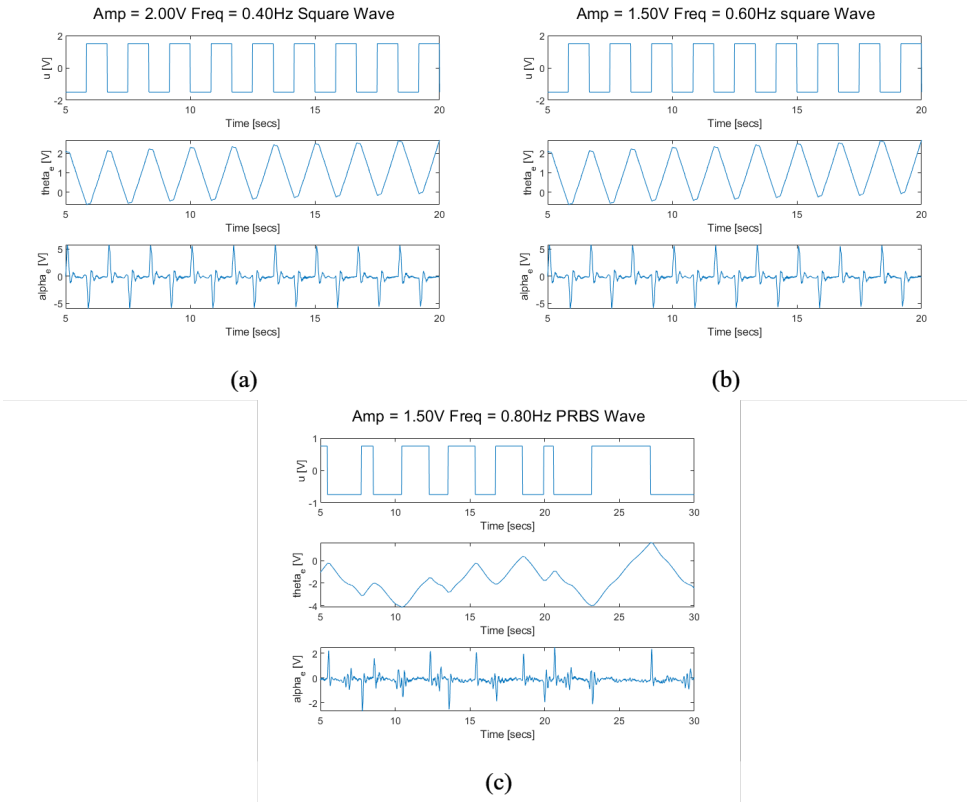

Figure 4: : (a) Square wave (Amp=$2V$), freq =$0.4H_z$), (b) Square Wave (Amp=$1.5V$), freq =$0.6H_z$), (c) PRBS Signal (Amp=$1.5V$), freq =$0.8H_z$)

3.2 Discussion of the sampling frequency. (1 pt)

We chose the sampling frequency carefully. Because the sampling rate should capture multiple harmonics in the output signal while allowing for enough samples per interval, more samples are typically better, however, excessive sampling can introduce noise and distort data, leading to inaccurate parameter identification. A sampling frequency of $\frac{1}{0.002}h_z$ was chosen for the experiment. We also kept in mind that the sampling frequency must be at least twice the highest frequency present in the signal, (known as the Nyquist rate), so that it can help prevent aliasing.

3.3 Effect on identification of filtering the data. (1 pt)

Filtering the data was crucial to reduce high-frequency noise and focus on the system's true dynamics. The motor's integrator, which causes continuous growth in the angular position, was removed by differentiating the motor shaft signal. This allowed the identification to concentrate on the flexible bar's behavior without the complicating effects of the motor's integrator.

A low-pass filter was applied to remove noise from the measurements, as the system's slow dynamics (due to inertia) are primarily in the low-frequency range. Detrending was also necessary to address any bias caused by the asymmetry of the excitation signals.

Choosing the right filter parameter, λ, was essential. If λ is too high, useful signal components are lost, resulting in poor model approximation and disappearing poles.

Conversely, if λ is too low, excessive noise is retained, which degrades the identification process. A balance must be struck to preserve the system's relevant dynamics while removing unnecessary noise.

3.4 Explanation on how the pole at the origin has been dwelt with. (0.5 pts)

The accurate parameter identification of the flexible arm requires addressing interference from a pole at the origin, caused by the motor system, which obscures the arm's behavior. In discrete systems, this pole acts as an integrator, appearing at $z = 1$.

To negate the integrator effect, the data is first differentiated, effectively removing the pole by modifying the system's transfer function $H(z)$:

$$H'(z) = (1 - z^{-1})H(z)$$

Following the identification of the system parameters, the pole is reintroduced by integrating the differentiated data:

$$H(z) = \frac{H'(z)}{1 - z^{-1}}$$

This technique ensures the identification process yields more accurate and reliable results for the flexible arm's parameters.

3.5 Discussion on how the model orders have been decided. Take into consideration that the plant results from the interconnection of a DC motor and the flexible bar and discuss the models needed for each of them. (1 pt)

In the ARMAX model, parameters were selected to precisely represent the system dynamics and effectively mitigate noise effects. The autoregressive order, denoted as $na = 3$ captures the influence of previous output values on current behavior. The exogenous input order, $nb = 2$, allowed the model to consider the two most recent inputs, while the moving average order, nc, was synchronized with $na = 3$, to adequately model the noise components influencing the output. Additionally, a pure time delay, $nk = 1$, reflects the inherent latency in the input's effect on the output. During the model calibration phase, various configurations with different numbers of expected poles were explored. However, these alterations invariably led to compromised model performance, characterized by reduced predictive accuracy and increased model complexity. Therefore, the selected parameters were affirmed as yielding the most favorable balance between model complexity and predictive precision for this specific application.

3.6 Description of the final ARMAX model. (0.5 pt)

The final model of the system was identified using an ARMAX structure, which combines autoregressive (AR), moving average (MA), and external input (X) components. The following parameters were selected for the ARMAX model based on experimental data:

- $na = 3$: The autoregressive (AR) part of the model, which captures the internal dynamics of the system based on past output values.
- $nb = 2$: The X part, which represents the system's response to the input signal u.
- $nc = 3$: The moving average (MA) part, which accounts for the noise dynamics, modeling past error values.
- $nk = 1$: The pure delay, indicating that there is a one-sample delay between the input and the system's response.

The transfer function obtained was:

$$H(z) = \frac{-0.010z + 0.021}{z^3 - 2.003z^2 + 1.199z - 0.179}$$

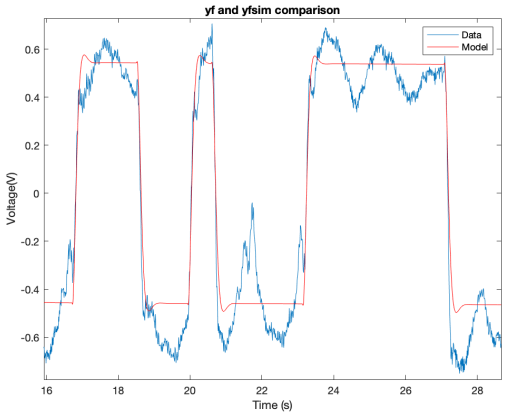

Comparison plot between the measured-filtered data and the simulated data

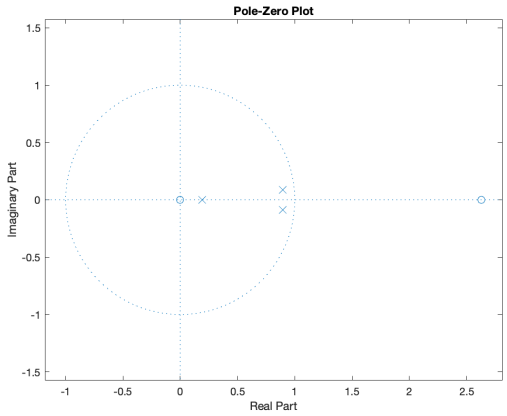

Pole-zero diagram

Figure 5: ARMAX plots

3.7 Description of the final state-space model. (0.5 pts)

The final state-space model was derived from the identified ARMAX model by incorporating an integrator.

Giving the following transfer function:

$$H(z) = \frac{-0.010z^3 + 0.021z^2}{z^4 - 3.004z^3 + 3.202z^2 - 1.378z + 0.179}$$

Then, we convert this function to state-space model giving the following result:

$$A = \begin{bmatrix} 3.004 & -3.203 & 1.378 & -0.179 \\ 1.000 & 0.000 & 0.000 & 0.000 \\ 0.000 & 1.000 & 0.000 & 0.000 \\ 0.000 & 0.000 & 1.000 & 0.000 \end{bmatrix} \qquad B = \begin{bmatrix} 1 \\ 0 \\ 0 \\ 0 \end{bmatrix}$$

$$C = \begin{bmatrix} -0.010 & 0.021 & 0 & 0 \end{bmatrix} \qquad D = 0$$

The state-space equations are given by:

$$\begin{aligned} x(k+1) &= Ax(k) + Bu(k) \\ y(k) &= Cx(k) + Du(k) \end{aligned}$$

3.8 Characterization of the plant open loop pole-zero plot, frequency response and time response of the model. (1.5 pt)

3.8.1 Pole-Zero Plot

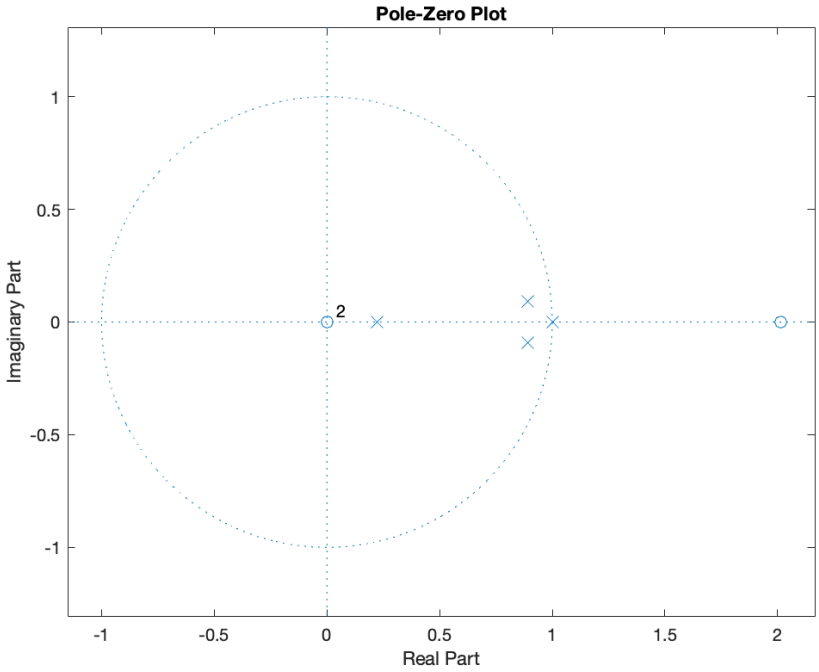

Figure 6: State space Pole-Zero Plot

Figure 6 shows that the system has four poles and three zeros. As we can observe, there is one zero located outside the unit circle. This phenomenon is physically noticeable at the precise moment when the motor changes direction, while the arm has not yet adjusted accordingly. Additionally, there is a pole exactly at $z = 1$ on the unit circle, indicating that the system is marginally stable. This marginal stability is characterized by the system's tendency to sustain oscillations or other behaviors that do not decay over time, due to the integrator effect.

3.8.2 Frequency Response

Here, the magnitude plot shows how the amplitude of the output signal changes with frequency. The phase plot shows the phase shift introduced by the system.

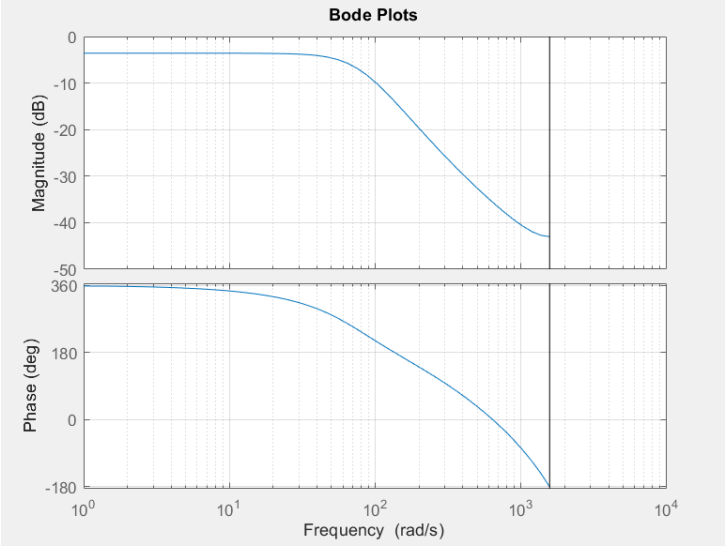

Figure 7: Bode Plot for the system

The Bode plot is not continuous to infinity because we had a discrete system. It ends around 1570 rad/sec because this is the Nyquist frequency for the given sampling time.

$$f_s = \frac{1}{T_s} = \frac{1}{0.002} = 500\,\text{Hz}, \quad f_{\text{Nyquist}} = \frac{f_s}{2} = 250\,\text{Hz}$$

$$\omega_{\text{Nyquist}} = 2\pi \times 250 = 1570.8\,\text{rad/sec}$$

The frequency response is limited by the Nyquist frequency to avoid aliasing.

3.8.3 Time Response

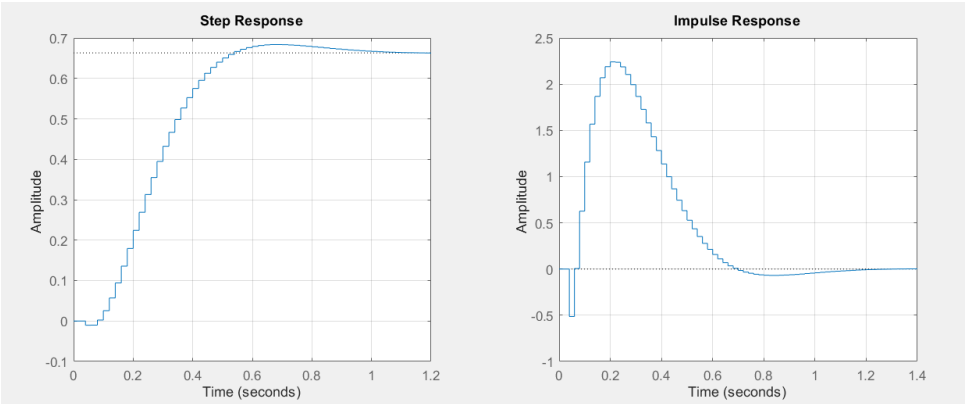

Figure 8: time response of the system

The step response shows the system's rise time, settling time, overshoot, and steady-state error. The impulse response describes how the system behaves when subjected to a very short input.

3.9 Model validation. (1.5 pts)

For model validation, we used the ARMAX model obtained with the PRBS data and tested it with square wave inputs at 0.6 Hz. The resulting graph is shown below.

The comparison of the model with the PRBS data yields a fit of 73%. On the other hand, when comparing the model to the square wave data y_f_square, we obtained a fit of 71%.

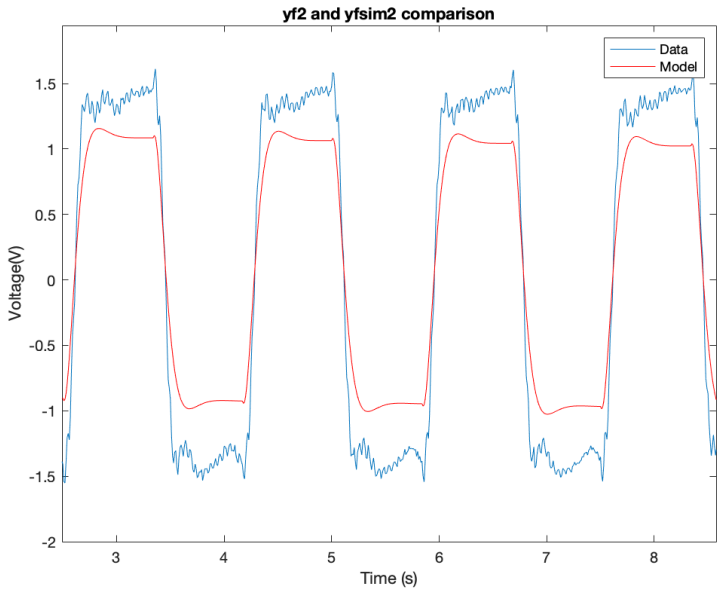

Figure 9: Model validation: Comparison of the previous ARMAX model with square wave inputs.

As a final validation we compared initial observation y with y_{dlsim}:

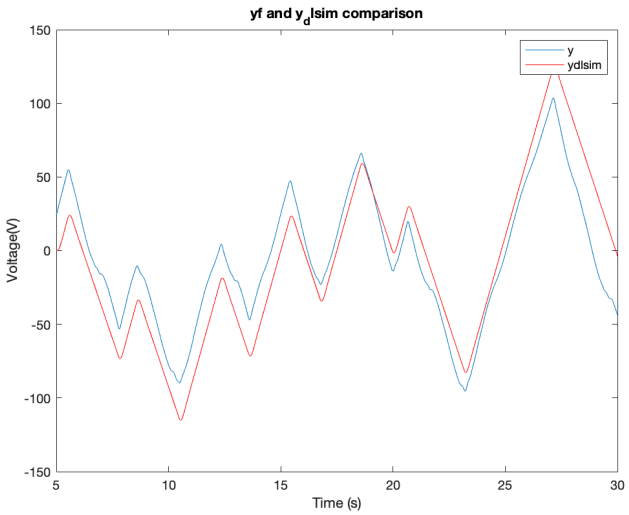

Figure 10: Model validation: Comparison of the previous ARMAX model with square wave inputs.